Paper:
Mouhamad, Y., Meroni, S., De Rossi, F., Baker, J., Watson, T., Searle, J. & Jewell, E. (2019). Geometrical optimization for high efficiency carbon perovskite modules. *Solar Energy, 187*, 129-136.
http://dx.doi.org/10.1016/j.solener.2019.05.047

Geometrical optimization for high efficiency carbon perovskite modules.

Y.Mouhamad, S. M. P Meroni, De Rossi, J. Baker, T. M. Watson , J. Searle, E. H. Jewell

SPECIFIC , College of engineering, Swansea University, Bay Campus, Engineering East, Crymlyn Burrows, Swansea, SA1 8EN

Abstract

The carbon based perovskite solar cell (C-PSC) has a strong commercial potential due its low manufacturing cost and its stability. A C-PSC consists of three mesoporous layers sandwiched between an FTO coated glass bottom electrode and carbon top electrode. The low conductivity of the two electrodes represents a challenge when scaling to modules. A 2D DC simulation is used to investigate the influence of cell geometry on the performance of a single C-PSC. It is also used to study the effect on performance of sub-cell width, interconnection width and interconnection contact resistance for a 10 sub-cells module. The carbon cell properties are taken form experimental J_{SC} and V_{OC} as model inputs. The carbon conductivity is critical in defining the optimum geometry. For a 10 Ω /sq carbon sheet resistance, the optimum interconnection width is 500 µm with a 4.9 mm sub-cell width, leading to a fill factor of 64 %.

Keywords: Carbon, perovskite, module, modelling, resistive losses

1. Introduction

Perovskite solar cells (PSC) have demonstrated significant power conversion efficiency (PCE) over the last 6 years(Kojima et al., 2009) from just over 3% to more recent reports at 23.7 % (Green et al., 2019). They have subsequently attracted attention as a promising candidate to compete with silicon-based and thin film PV technologies.

Among the numerous PSC architectures reported so far, a hole transport material (HTM)-free mesoscopic stack, including overlapping titania, zirconia and carbon , Figure 1 (Mei et al., 2014), has been regarded as a promising means of commercial exploitation (Yang et al., 2017). The carbon

electrode architecture is often referred as carbon perovskite solar cell (C-PSC). Although the highest C-PSC reported at 17 % (Lui et al., 2017) is below the state of the art PSC, the C-PSC neither requires expensive HTMs, such as Poly[bis(4-phenyl)(2,4,6-trimethylphenyl)amine (PTAA), poly(3-hexylthiophene-2,5-diyl) (P3HT) and Spiro-OMeTAD, nor does it require the use of evaporated noble metals, such as gold and silver. In addition, this architecture is fully printable with conventional high throughput mature low cost manufacturing techniques, such as screen printing (Meroni et al., 2018; Poli et al., 2018) and inkjet printing (Hashmi et al., 2017). C-PSCs have been successfully up-scaled to modules, delivering up to 11 % PCE on 10 x 10 cm substrates (Hu et al., 2017; Priyadarshi et al., 2016) and over 6 % PCE on A4-sized substrates (De Rossi et al., 2018a), showing also stability under continuous illumination (Grancini et al., 2017), in outdoors (Hu et al., 2017) and when exposed to humidity (De Rossi et al., 2018b).

The poor conductivity of the FTO and carbon electrodes limits a further performance improvement for large scale C-PSC modules and requires careful design to overcome. A 'sub-cell design' is used with series connection of individual cells to minimise resistance related losses (Krebs et al., 2007). This 'sub-cell' design has to maximise the dimensions of the active area and minimizing the dimension of the non-active area, including the interconnection area, whilst still minimizing the resistive losses. The design of the module also depends on the coating deposition technique and the method used to create electrical connection between two consecutive sub-cells and isolation between two consecutive top and bottom electrode. The majority of C-PCS modules (De Rossi et al., 2018a; Hu et al., 2017; Priyadarshi et al., 2016) reported using the registration method (see Figure 2b). This consists of overprinting the titania, zirconia and carbon to isolate them from one another and from the adjacent sub-cells. Similarly, the electrical connection between two adjacent sub-cells is obtained by printing carbon on FTO. The poor conductivity of the carbon and the FTO requires wide connections which results in wide inter-cell distance which in its turn reduces the geometrical fill factor (GFF, ratio between active area and total area).

An alternative manufacturing strategy is the scribing method (see Figure 2a), which is commonly used for other module architectures (Galagan et al., 2012). This method uses laser scribing or mechanical scribing to selectively remove deposited layers to isolate the top and bottom electrodes of two successive sub-cell and create a path to electrically connect the sub-cells. The method results in finer sub-cell distance and which leads to higher geometrical fill factor [13]. For a highly conductive top electrode, such as gold, the width of the interconnection can be minimised to typically 200 µm (Palma et al., 2017; Yang et al., 2018). However, in the case of the C-PCS, such a fine interconnection will result in significant resistive losses due to the conductivity of the carbon, representing the limiting factor in the stack. For a given sub-cell width there will be an associated interconnection width for which the module efficiency will be optimised. Numerical modelling techniques have been used to find the optimum module dimensions for other perovskite architectures (Galagan et al., 2016; Rakocevic et al., 2017) and other PV technologies (Malm, 2008; Van Deelen et al., 2014), however, these studies have ignored the significant resistive nature of the rear electrode, a factor which is unique in the carbon perovskite module. Thus, C-PSC module optimization requires consideration of both the cell width and the interconnection width (P2) to achieve the maximum power output.

Here we use 2D electrical modelling to study the effect of the active area on performance of a single C-PSC cell. We then investigate the optimal dimensions of the C-PSC module fabricated using the scribing method by studying the effect of the sub-cell width, the width of carbon / FTO interconnection and the contact resistance at that interface. Since the lab scale devices for this architecture have significant series resistance, we use 'ideal cell data' neglecting series resistance as input to our model and then incorporate the series resistance based on sheet and contact resistances for the carbon and FTO contacts. Experimental and theoretical aspects of the investigation are discussed and this work takes a step forward in evaluating the scaling lag (Carlé et al., 2017) of perovskite solar cells which must be reduced in order to commercialise this technology.

2. Method

2.1 Experimental method

The cell creation utilized a standard laboratory manufacturing procedure developed in the laboratory (Baker et al., 2017; Meroni et al., 2018). The FTO substrate was cleaned with a solution of cleaning liquid Hellmanex then rinsed with Acetone, then isopropyl alcohol (IPA). The substrates were then plasma treated for 10 minutes. A compact TiO_2 layer was spray coated from a solution with 10 % Titanium diisopropoxide bis (acetylacetonate) dissolved in IPA. The layers were then dried at 300 °C for 25 minutes. Dyesol 30NR-D paste was diluted 1:1 in terpineol to make the paste to screen print the mesoporous titania layer. This layer was sintered at 550 °C for 30 minutes. The mesoporous zirconia layer was screen printed and heat treated at 400 °C for 30 minutes. The carbon was then screen printed with a D3 paste manufactured by Gwent Electronic Materials which was found to provide optimum high conductivity and process-ability(Philip et al., 2016). The layer was first dried at 100 °C then heat treated at 400 °C to create the porous structure. The infiltration of the perovskite was performed in a controlled cleanroom (30 % RH, 21 ^{o}C). The perovskite was prepared by dissolving 439.0 mg/mL PbI_2, 151.4 mg/mL CH_3NH_3I (MAI), and 6.7 mg/mL $NH_3(CH_2)_4COOH$ I (AVAI) in γ-Butyrolactone. 8 µl was then deposited on the active area of the cell. The cells were then kept in the fume hood for 10 min and then placed in the oven at 50 °C for 60 min. To reduce contact resistance at the point of contact, the edges of the substrate are taped with kapton tape. The cells manufactured had a dimension of 10 × 20 mm, a mask of 7 × 7 mm reduces the illuminated area to 49 mm^2.

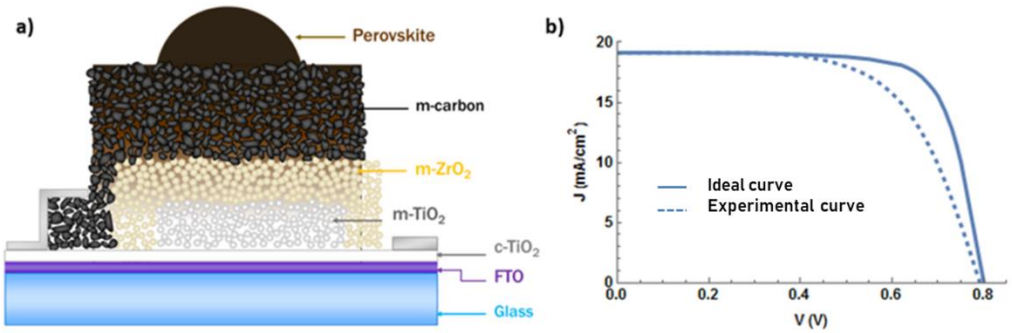

Figure 1: a) Architecture of a single cell. b) Dashed line J-V curve obtained on a cell 49 mm^2, solid line hypothetical curve used for modelling

The dashed curve one Figure 2b, shows the characteristics of the smallest cell we could manufacture (49 mm^2) using the same material and scalable screen printing process. The cell shows high shunt resistance and also significant series resistance, which limits the fill factor to 62 %.

2.2 Strategy

When modelling the characteristics of the C-PSC module the input to model required an experimental JV characteristics of a cell sufficiently small (< 2 mm^2) that resistive losses can be neglected. However, the manufacturing process of the C-PSC does not allow the fabrication of such small cell and despite the measures taken the significant restive losses leads to a low fill factor (see dotted line in Figure 1b). Therefore the J_{SC} and V_{OC} of the JV curve used to perform the modelling were based on the experimental results , whereas the fill factor was estimated using literature (Green et al., 2019) to create an idealised JV curve with limited series resistance losses (see solid line in Figure 1b). This provided cell performance with the material which is fully compatible with scalable manufacture (Priyadarshi et al., 2016). This was used to investigate the effect of C-PSC cell geometry and subsequently an entire C-PSC module.

2.3 Theoretical modelling

2.3.1 Single Cell

To model the resistive losses of cell a 2D direct current modelling approach was used which assumes that there is no voltage drop along the length of the cell. Two types of resistive losses are considered: the voltage drop across each individual electrode and the potential difference between the top and bottom electrodes. The bottom electrode was commercially available FTO glass substrate with a sheet resistance of 7 Ω/sq. The top electrode is a screen printed mesoporous carbon layer, whose sheet resistance post high temperature annealing was measured to be 10 Ω/sq for a thickness of 10 µm. The potential distribution in the surface was modelled using:

$$\nabla \frac{1}{R_{Carbon}} \nabla V_{carbon} = -J_A(\Delta V), \qquad \text{Equation 1}$$

$$\nabla \frac{1}{R_{FTO}} \nabla V_{FTO} = J_A\,(\Delta V)\,. \qquad \text{Equation 2}$$

Where R_{Carbon} is the sheet resistance of the carbon electrode (10 Ω/sq), R_{FTO} is the sheet resistance of the FTO (7 Ω/sq), V_{carbon} , the electrical potential at the carbon electrode ,V_{FTO} the electrical potential of FTO electrode, J_A is the current density passing through the two electrodes. It accounts for the intrinsic properties of the mesoporous carbon cell. Here J_A is the idealised current density (see solid line in Figure 1b). $J_A\,(\Delta V)$ depends on ΔV which is the electrical potential between the carbon and the FTO electrode:

$$\Delta V = V_{FTO} - V_{Carbon}. \qquad \text{Equation 3}$$

An electrical potential ranging from 0 V to 1 V is applied at the carbon electrode, a ground is applied on the FTO substrate and the voltage drop across the module is computed. The power, the short circuit current, the open circuit voltage and the fill factor are all derived from the current density which is defined as

$$J_{cell} = \frac{1}{A_T} \int J_A \; dA_A. \qquad \text{Equation 4}$$

Where A_A is the active area of the cell and A_T the total area of the substrate. The modelling was carried out using COMSOL Multiphysics AC/DC module. The geometry were generated in AutoCAD 2017 and the processing of the data was carried out in Mathematica 10.

2.3.2 Module

The model consisted of a module with 10 sub-cells connected in series. Each sub-cell is characterised by the width of the active area of the sub-cell (W_{Sub}), the electrical insulation and electrical connection implemented with the P1, P2, P3 scribes (see Figure 2). P1 is the cut on the FTO, which enables isolation of each sub-cell. P2 is the channel created inside the compact titania and the mesoporous layers. It is then filled with carbon to create a contact with the FTO and connect to the next cell. The P3 scribe removes the top carbon electrode and the mesoporous layers to isolate the sub-cells. The spacing separating P1 to P2, and P2 to P3 are referred to as S1 and S2, respectively. P1, P3, S1 and S2 are fixed and a parametric sweep is performed on P2 and W_{Sub}. In this instance it is assumed that P1 is done via laser scribing whereas the P2 and P3 are scribed mechanically. This combination of scribing techniques reflect our current laboratory capability. P1 was set to 50 μm and P3 to a larger value of 250 μm as the resolution of the mechanical scribing depends on width of the blade, which inherently produces a wider gap than a laser. S1 and S2 are both set to 200 μm as this represents our current best practice in the laboratory.

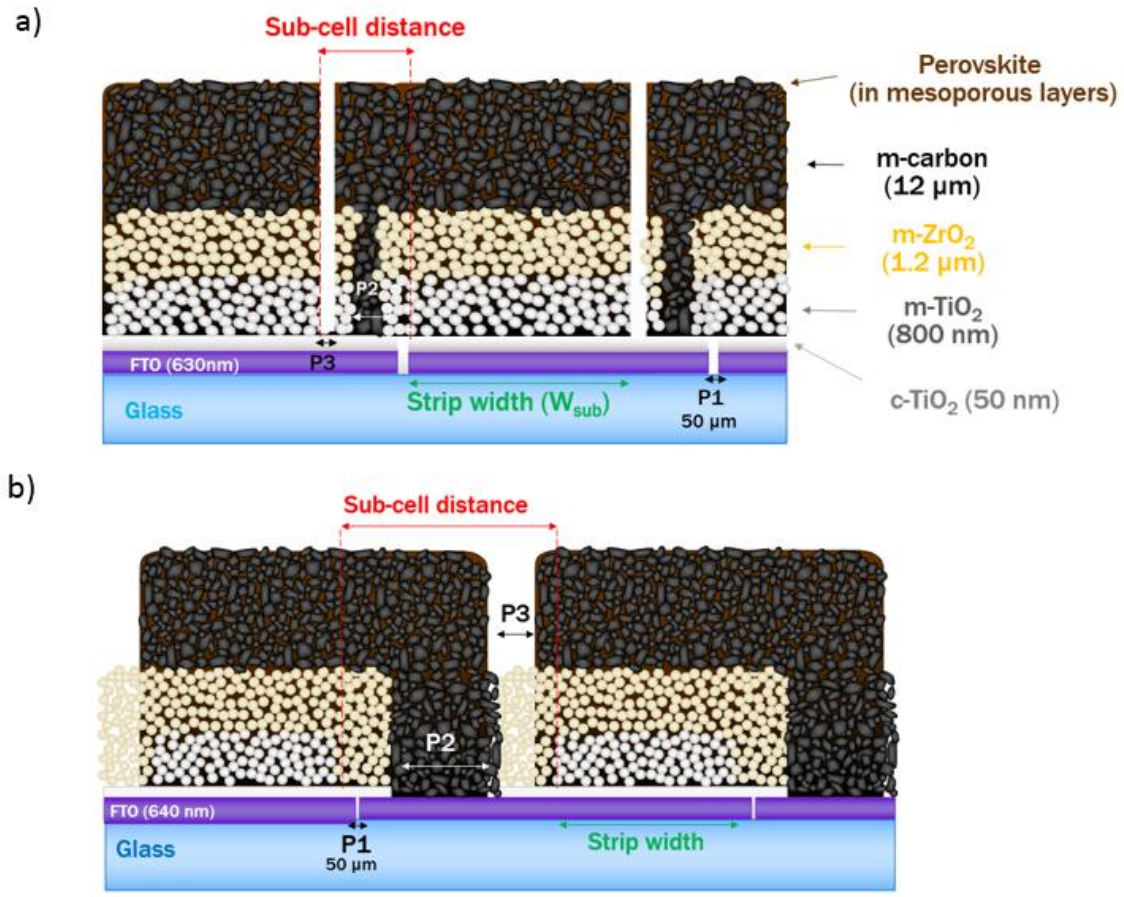

Figure 2: a) Architecture of module of a module with scribing method, b) architecture of a modulw with the registration method: P1 and P3 are the isolation of the sub-cell from the bottom and top electrode, respectively. P2 is the electrical interconnection between the cells

The model to simulate the performance of the module follows the same approach than the model for single cell. Two Poisson equations are solved at the two electrodes. The current density passing at a given point on the module depends on the electrical difference between the two electrodes. To account for the contact resistance at the interconnection, the current density lost due to the contact resistance is subtracted from the total current density

$$J_{Carbon\ @int} = -J_{FTO\ @int} = -\frac{\Delta V}{R_{contact}}. \qquad \text{Equation 5}$$

Here $R_{contact}$ is the contact resistance between the FTO and the carbon, i.e. 0.06 Ω (De Rossi et al., 2018), $J_{Carbon\ @int}$ is the current density at the interconnections on the carbon electrode and $J_{FTO\ @int}$ is the current density at the interconnections on the FTO electrode. An input voltage is

sweep of 0 V to 10 V is applied at the carbon electrode while a ground is applied at the FTO. The model is solved for the electrical potential map at the two electrodes. Once the computation has ended, for a given input voltage one can visualise the electrical potential map of the carbon electrode, top electrode and the potential difference between the two electrode by plotting V_{Carbon}, V_{FTO} and ΔV, respectively.

3. Results

3.1 Single cell

For a single cell, the influence of the geometry can be examined by studying the performance of a cell with a width (W) ranging from 0.5 mm to 20 mm. As can be expected, the performance of the cell decreases with increased cell width due to the increased resistance of the carbon and FTO, Figure 3(a). Between the range of 0.5 mm and 15 mm, the short circuit current (J_{SC}) is largely unaffected by the cell's width, Figure 3(b). However, beyond a width of 15 mm the J_{SC} decreases. At a given point on the cells, the potential gradient on the two electrodes depends on the resistivity of the electrodes via equation 1 and equation 2. The current density flowing through that point depends on the differential potential between the top and bottom electrodes. As the width of the active area widens, the voltage drop across the individual electrodes increases which results in a higher potential difference between the top and bottom electrodes and hence leads to a lower current flowing through the cell.

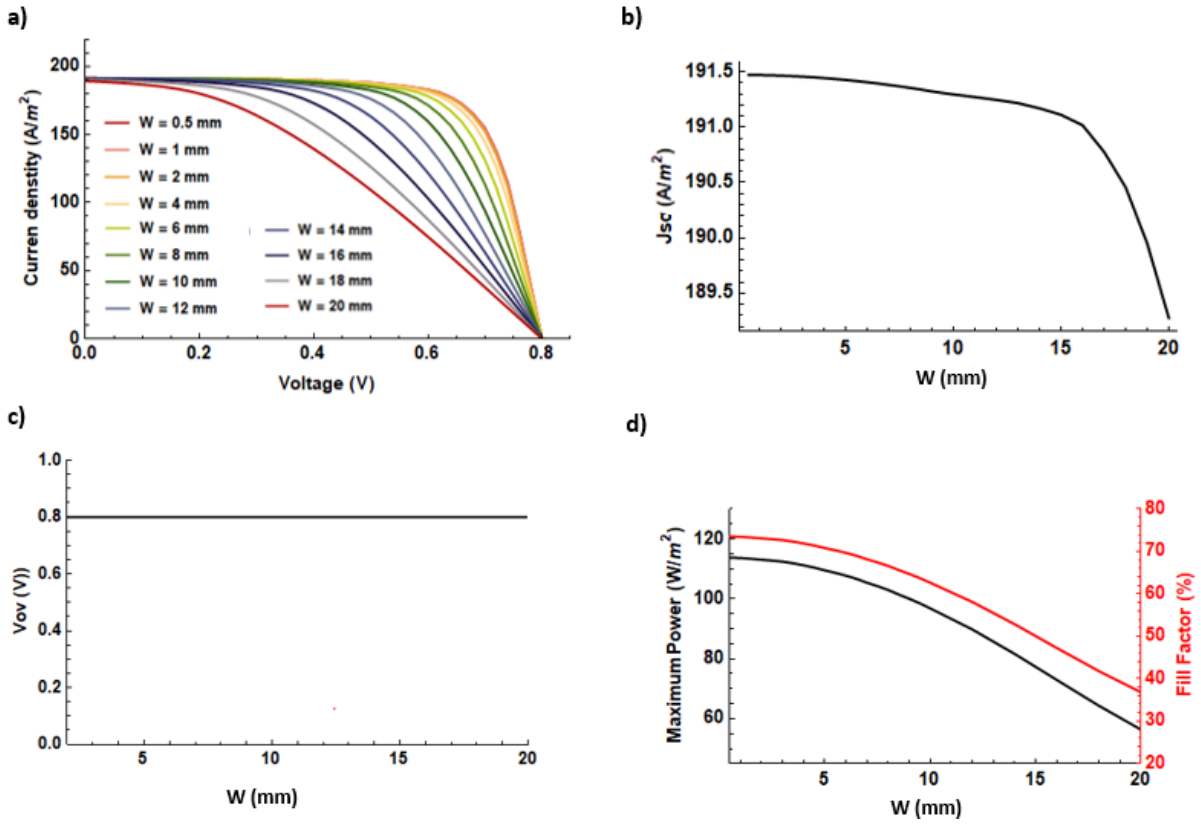

Figure 3: PV characteristics for a single cell. a) J-V curves, b) J_{SC}, C) V_{OC}, d) Maximum power output and fill factor, as a function of the cell's width

The open circuit voltage is independent on the width of the active area, see Figure 3c. This is expected, as the V_{OC} solely depends on the materials chemistry of the cell and the recombination phenomena, which are not considered in this work. The maximum power generated, and the fill factor decreases as the width of the active area is widened, see Figure 3d. In addition, when the sub-cell width is wider than 5 mm, the maximum power reaches a critical point at which it decreases at a significantly faster rate than previously. It implies that beyond this value the benefit of additional area is negated by the increased electrode resistance. To maintain a fill factor of above 70 %, cells should be no wider than 5 mm.

3.2 Module

To determine the optimum W_{Sub} and the optimum P2 for which the performance of a module with 10 sub-cells is optimised, a parametric sweep of W_{Sub} and P2 was carried out, while keeping P1, P3, S1 and S2 constant. The modelling of the single cell establishes that an active area larger than 10 mm experiences significant resistive losses which then affect the FF and thus the maximum output power. For this reason, the sub-cell widths studied ranged from 2 mm to 10 mm. The interconnection width is varied from 50 µm to 2 mm.

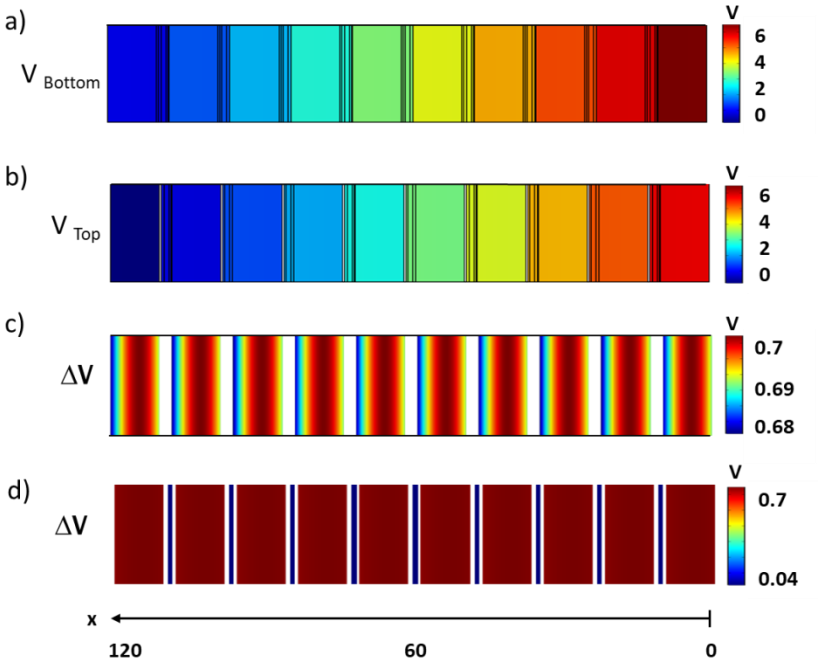

Figure 4: Electrical potential map on the bottom electrode a), and the top electrode b). Difference between the bottom and top electrode ΔV c) active area , and d) active area and interconnection P2.

Figure 4 shows the electrical potential map of a 10 sub cells module with a W_{Sub} =5 mm and a P2 = 500 µm. A potential (6 V) is applied at the bottom electrode of the first sub cell, the current flows to the top electrode of the last sub cell via the interconnection (Figure 4a and 4b). The electrical potential at the bottom electrode is higher than the one on the bottom electrode. This is clear on Figure 4a and 4d where ΔV is positive. Note that ΔV is higher on the active area than at the interconnection, this is expected as the two electrodes are in contact at the interconnection. The potential difference at the interconnection is not null as it accounts for the contact resistance.

The results for a module of 10 cells serially connected provide an insight into the geometric trade off, Figure 5; note that the characteristics reported for the total area of the module, not just the active area. Figure 5a shows the maximum power achieved as function of P2, and the W_{Sub}. The zones in red highlight the extreme cases: high values of P2 (1.5 mm to 2 mm) for relatively small active area and small P2 width for relatively large sub-cell width. For P2 ranging from 50 µm to 100 µm the maximum power decreases rapidly when the sub-cell width increases. This is more clearly visible in Figure 5b, in that at low ranges of P2 the maximum power is limited by resistive losses at the interconnection which limits the current that transfers between subsequent sub-cells. As the size of the P2 increases, the resistive losses decrease, and the maximum power achieved increases. For a given P2 there is an optimum sub-cell width for which the maximum power is maximised. Beyond that sub-cell width the maximum power generated by the module decreases and its performance is limited by the sub-cell width. For a given P2, the maximal maximum power achievable are denoted by the black dots in Figure 5b. These are reported in Figure7, it is clear that the optimum sub-cell width increases with increasing P2. As P2 increases the losses over the interconnections increases and the active area needs to generate more charges and compensate the losses at the interconnection.

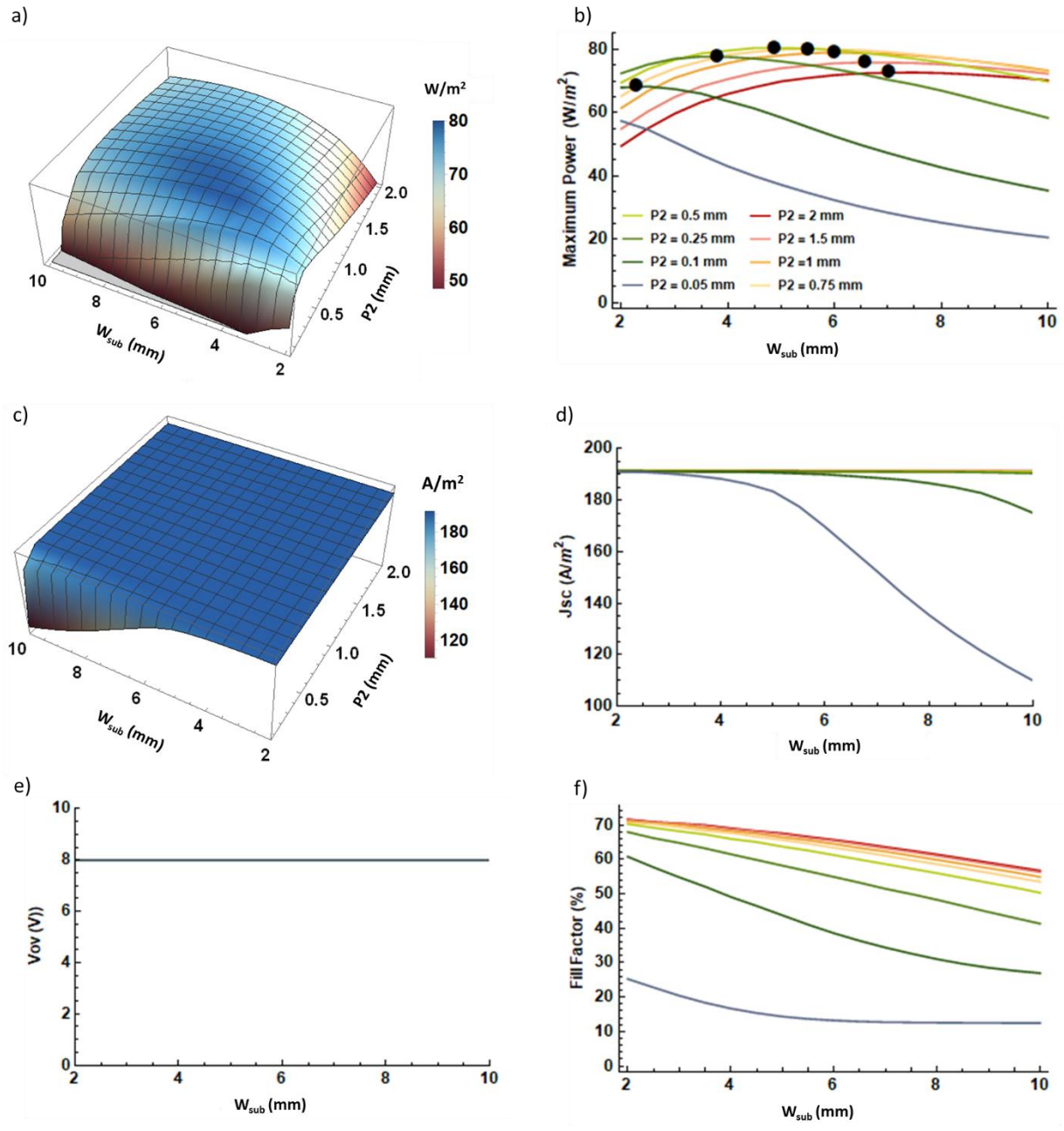

Figure 5: PV characteristics of module made of 10 sub-cells connected in series for a carbon layer with a sheet resistance of 10 Ω/sq and contact resistance of 0.06 Ω at the interconnection. a) 3D plot of P_{max} as function of P2 and the sub-cell width, b) P_{max} as a function of sub-cell width for different P2. c) 3D plot of J_{SC} as function of P2 and the sub-cell width, d) J_{SC} as function of the sub-cell width for different P2values. (e) V_{OC} as function of the sub-cell width for different values of P2. f) FF as function of the sub-cell width for different values of P2.

For P2 widths above 100 µm the J_{SC} is constant and equal to the J_{sc} of single cell, Figure 5c. For P2 equal to 50 µm and 100 µm there is a given sub-cell width for which the J_{sc} drops significantly, 3.5 mm for P2= 50 µm and 6 mm for 100 µm. Although the J_{sc} of a module connected in series should be

equal to that of the single cell, for such small P2 the losses are such that they limit the current flow. As it would be expected from a module connected in series the V_{OC} is independent of the width and equal to 8 V which is the V_{OC} of the singles cell multiplied by the number of cells, Figure 5c.

Wider P2 widths (>750 µm) have little impact on the fill factor. In these wide ranges of P2 the gain obtained from having a wider P2 is counter balanced by the fact that the charges must travel a longer distance to reach the following sub-cell hence the convergence of the curves. However, with the thinnest scribes of P2 = 50 µm, the interconnection limits the power generated by the module which then results in poor fill factor with a weak dependence on the sub-cell width , Figure 5d. Between P2 widths of 100 µm to 250 µm the fill factor increases significantly and the dependence in the sub-cell width is less pronounced.

The optimum performance is obtained for a P2= 500 µm, a sub-cell width width of 4.9 mm which results in a fill factor of 65.5 %. Comparing Figure 3 and Figure 5, the performance a single cell improves as the sub-cell's width get smaller, however for modules the poor conductivity of the two electrodes, and losses at the interconnection, wide sub-cell width are necessary to compensate the loses. This optimum design, compares favorably with the module design for a perovskite module which used FTO as bottom electrode and gold as the top electrode (Palma et al., 2017) . Palma *et al.* modelled the module geometry for the state of art perovskite stack which has a gold as top electrode. They predicted an optimum of P2 width of 192 µm and an optimum sub-cell width of 6.87 mm. Hence an electrode with higher conductivity allows for wider sub-cell which enhances the current generated as well as a fine P2 which improves the fill factor. However due to the limitation of the laser used, Palma *et al*. chose a P2 of 213 µm.

3.3 Ideal case of a more conductive carbon and no contact resistance

Priyadarshi *et al* (Priyadarshi et al., 2016) demonstrated experimentally the impact of the carbon's conductivity on the performance of C-PSC module by manufacturing modules with inks with sheet resistance of 40 Ω/sq, 15 Ω/sq, and 8.5 Ω/sq. An increase of 8 % in the PCE was reported between the least conductive carbon and the most conductive carbon. Since the impact of carbon conductivity was found to alter the ideal module geometry and output characteristics, a theoretical study was carried out to examine the impact of the sheet resistance. In practice this could be achieved by using a higher conductivity material or a thicker film. The same analysis method was used with the sheet resistance of the carbon paste set to 8.5 Ω/sq and zero contact resistance at the FTO / carbon interface. The implementation of the modelling is similar to that reported in section 3.2, except that at the ideal contact at the interconnection translates mathematically into

$$\Delta V = 0. \qquad \text{Equation 6}$$

This implies that at the interconnections there is no voltage drop between the top and the bottom electrode. The values of P1, P3, S1 and S2 are unchanged. The performance of the more conductive carbon electrode is illustrated in Figure 6 while a direct comparison of the maximum power output and optimal sub-cell width are given in Figure 7.

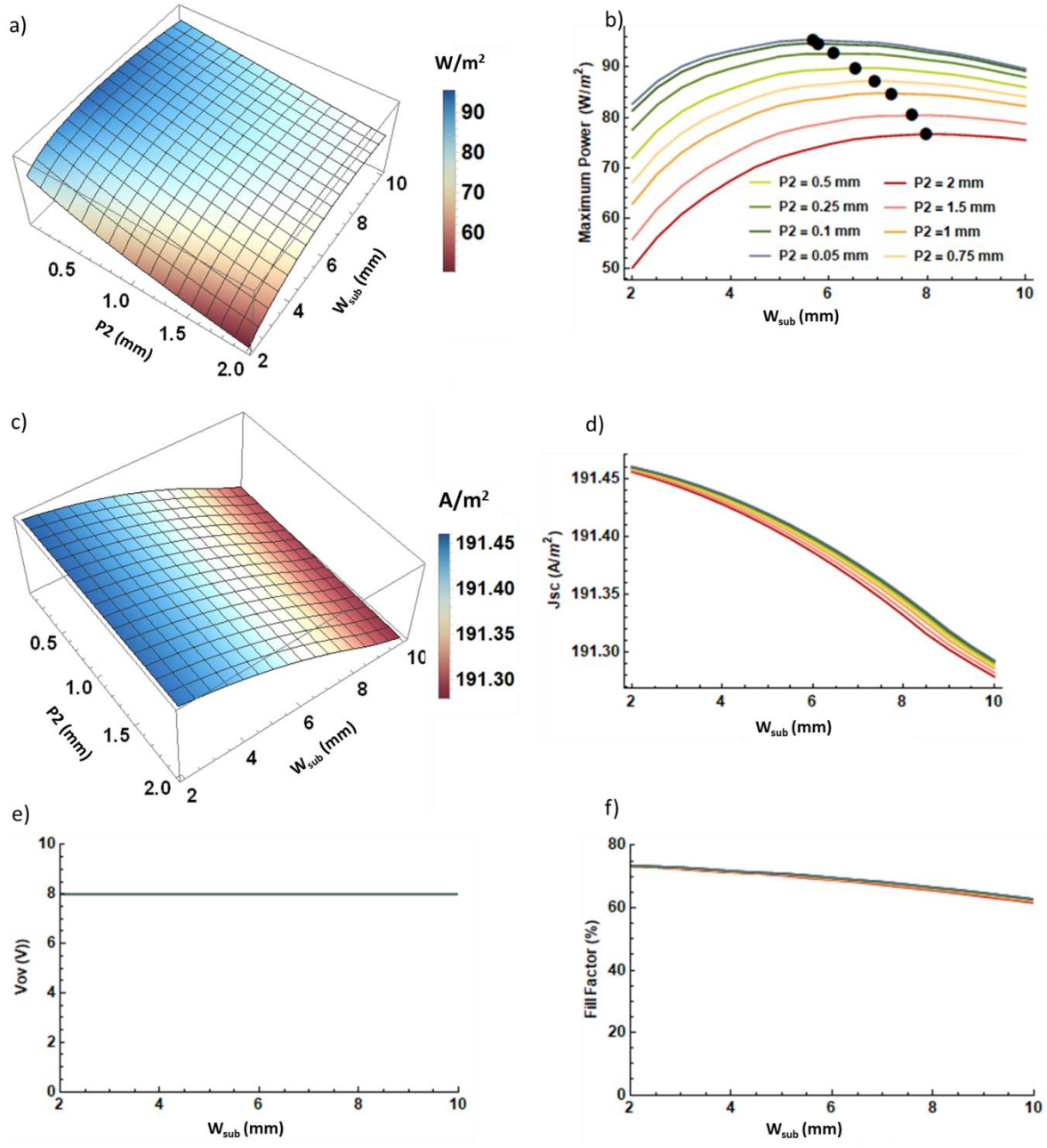

Figure 6: Characteristics of a module with 10 serially connected sub-cells and a carbon ink with a sheet resistance of 8 .5 Ω/sq and no contact resistance at the interconnection. a) 3D plot of P_{max} as function of P2 and the sub-cell width, b) P_{max} as a function of the sub-cell width for different P2 values. c) 3D plot of J_{SC} as function of P2 and the sub-cell width, d) J_{SC} as function of the sub-cell for different P2 values. e) V_{OC} as function of the sub-cell width for different values of P2. f) FF as function of the sub-cell width for different values of P2

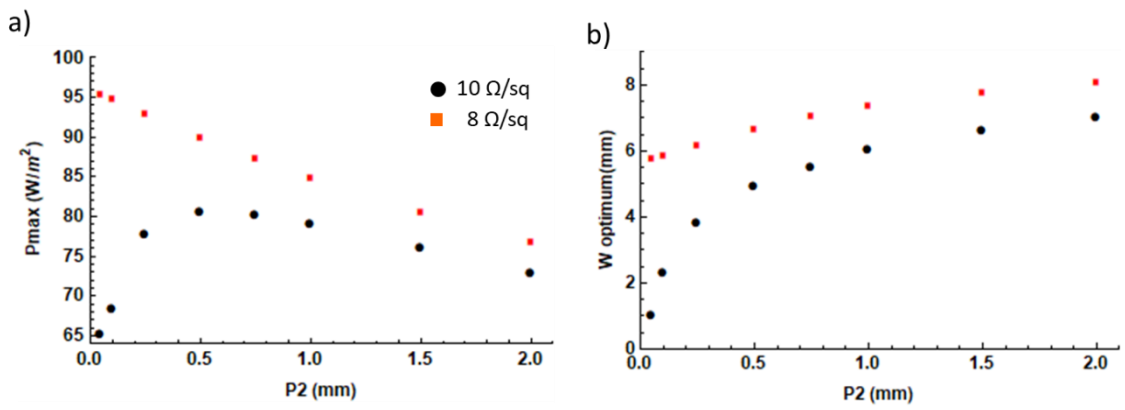

Figure 7: Dependence of a) P_{max} and b) optimum sub-cell width on the P2 for modules with carbon layers of 10 Ω/sq including contact resistance and 8 Ω/sq and zero contact resistance

For a given P2, the maximum power output achieved with the 8 Ω/sq carbon is consistenltly higher than the maximum power output achieved with the 10 Ω/sq. In Figure 6b regardless of the P2 , there is a window of W_{Sub} over which the power is maximised. This is in line with the wider window of sub cell width reported for a gold electrode (Galagan et al., 2016) but it is in contrast with Figure 4b where the power is maximised at a specific value of W_{Sub}. The limited conductivity of the 10 Ω/sq carbon and the contact resistance gives a limited range of sub-cell width over which the efficiency of the cell is optimal, this suggests that more conductive carbon materials leaves a wider margin for error on the accuracy of the width of the sub-cell. Figure 7b show a step wise increment of the optimum W_{sub} as the P2 width is increased. However, for the 10 Ω/sq carbon the optmial subcell width drops from 7 mm for a P2 of 2 mm to 1 mm for a p2 of 50 µm. This drop is less significant for the 8 Ω/sq , it drops from 8.2 mm for a P2 of 2 mm to 5.8 mm for a p2 of 50 µm . Hence, the effect of the P2 on the optimum sub-cell width becomes less significant for more conductive carbons. In Figure 7b regardless of the value of P2 the 8 Ω/sq carbon has a wider optimum sub-cell width than the 10 Ω/sq carbon. As a result for a given size substrate the manufacturing of a module with an 8 Ω/sq carbon will require less scribing than that of a module with a 10 Ω/sq carbon. Hence, high conductive carbons have the double benefit of increasing yield while reducing the processing time

From Figure 6d and Figure 6e one can see that J_{sc} and the fill factor have a weak dependence on the subcell width, and they are independent of P2 as all the curves converge. The absence of a maximum in the surface on Figure 6a suggests that the optimum P2 is finer than 50 µm. However, It would be technically challenging to mechanically scribe a clean sub 50 µm through four layers and then fill the gap with a carbon paste. In addition, Figure 6d shows that there is very little gain in having a P2 of 50 µm compared to a P2 of 250 µm. Hence from a manufacturing prospective a P2 of 250 µm and a W_{sub} of 6.3 mm will be ideal. This will result in a fill factor of 70% , this value could potentailly be enhenced if the widths of S1, S2 and P3 can / could be decreased.

The conductivity of the carbon, which is often overlooked in the small cell device community, is critical to the overall performance characteristics of the module. Although it's primary role is only to extract charges from the cell, this study clearly demonstrates its relevance and why the development of more conductive carbons is essential for the commercialisation of carbon perovskite module.

4. Conclusion

The effect of the resistive losses on the scaling up of the carbon stack including the contact resistance at the FTO / carbon interface was studied. For a carbon with a conductivity of 10 Ω/sq a sub-cell of 4.9 mm and P2 of 500 µm are optimum, this width of P2 scribe is within the capabilities of both a mechanical and laser scribe. The ideal case of an 8 Ω/sq carbon and a perfect contact at the FTO/ Carbon interconnection, revealed wider sub-cell width (5.5 mm) and smaller P2 (50 µm) are necessary to optimize the efficiency of the module. 50 µm scribes are not achievable with mechanical scribing, hence the benefits of having a higher conductivity carbon will be maximised when the mechanical scribing will reproducibly achieve a scribe similar than those achieved with a

laser. In addition to enhancing performance of the module, higher conductive carbons also reduce processing time while maintaining yield and allow for a greater manufacturing tolerance on the width of the sub-cell.

Funding sources

This work was made possible by the support given to the SPECIFIC Innovation and Knowledge Centre by the Engineering and Physical Science Research Council [EP/N020863/1], Innovate UK [920036], Engineering and Physical Science Research Council [EP/N509905/1] and by the European Regional Development Fund [c80892] through the Welsh Government.

References

Baker, J., Hooper, K., Meroni, S., Pockett, A., McGettrick, J., Wei, Z., Escalante, R., Oskam, G., Carnie, M., Watson, T., 2017. High throughput fabrication of mesoporous carbon perovskite solar cells. J. Mater. Chem. A. 35, 18643–18650. https://doi.org/10.1039/C7TA05674E

Carlé, J.E., Helgesen, M., Hagemann, O., Hösel, M., Heckler, I.M., Bundgaard, E., Gevorgyan, S.A., Søndergaard, R.R., Jørgensen, M., García-Valverde, R., Chaouki-Almagro, S., Villarejo, J.A., Krebs, F.C., 2017. Overcoming the Scaling Lag for Polymer Solar Cells. Joule. 1, 274–289. https://doi.org/10.1016/j.joule.2017.08.002

De Rossi, F., Baker, J.A., Beynon, D., Hooper, K.E.A., Meroni, S.M.P., Williams, D., Wei, Z., Yasin, A., Charbonneau, C., Jewell, E.H., Watson, T.M., 2018. All Printable Perovskite Solar Modules with 198 cm2 Active Area and Over 6% Efficiency. Adv. Mater. Technol. 3, 1–9. https://doi.org/10.1002/admt.201800156

Galagan, Y., Coenen, E.W.C., Sabik, S., Gorter, H.H., Barink, M., Veenstra, S.C., Kroon, J.M., Andriessen, R., Blom, P.W.M., 2012. Evaluation of ink-jet printed current collecting grids and busbars for ITO-free organic solar cells. Sol. Energy Mater. Sol. Cells. 104, 32–38. https://doi.org/10.1016/j.solmat.2012.04.039

Galagan, Y., Coenen, E.W.C., Verhees, W., Andriessen, R., 2016. Towards scaling up of perovskite solar cells and modules. J. Mater. Chem. A 4, 5700–5705. https://doi.org/10.1039/C6TA01134A

Grancini, G., Roldán-Carmona, C., Zimmermann, I., Mosconi, E., Lee, X., Martineau, D., Narbey, S., Oswald, F., De Angelis, F., Graetzel, M., Nazeeruddin, M.K., 2017. One-Year stable perovskite solar cells by 2D/3D interface engineering. Nat. Commun. 8. https://doi.org/10.1038/ncomms15684

Green, M.A., Emery, K., Hishikawa, Y., Warta, W., Dunlop, E.D., Levi, D.H., Ho-Baillie, A.W.Y., 2019. Solar cell efficiency tables (version 53). Prog. Photovoltaics Res. Appl. 27, 3–12. https://doi.org/10.1002/pip.2855

Hashmi, S.G., Martineau, D., Li, X., Ozkan, M., Tiihonen, A., Dar, M.I., Sarikka, T., Zakeeruddin, S.M., Paltakari, J., Lund, P.D., Grätzel, M., 2017. Air Processed Inkjet Infiltrated Carbon Based Printed Perovskite Solar Cells with High Stability and Reproducibility. Adv. Mater. Technol. 2, 1600183. https://doi.org/10.1002/admt.201600183

Hu, Y., Si, S., Mei, A., Rong, Y., Liu, H., Li, X., Han, H., 2017. Stable Large-Area (10×10 cm^2) Printable Mesoscopic Perovskite Module Exceeding 10% Efficiency. Sol. RRL. 1. 1600019. https://doi.org/10.1002/solr.201600019

Kojima, A., Teshima, K., Shirai, Y., Miyasaka, T., 2009. Organometal Halide Perovskites as Visible-Light Sensitizers for Photovoltaic. J. Am. Chem. Soc. 131.6050–6051.

Krebs, F.C., Spanggard, H., Kjær, T., Biancardo, M., Alstrup, J., 2007. Large area plastic solar cell modules. Mater. Sci. Eng. B Solid-State Mater. Adv. Technol. 138, 106–111.

https://doi.org/10.1016/j.mseb.2006.06.008

Malm, U., 2008. Modelling and Degradation Characteristics of Thin-film CIGS Solar Cells, Acta Universitatis Upsaliensis. Digital Comprehensive Summaries of Uppasala Dissertations From the Factulty of Science and Technology.

Mei, A., Li, X., Liu, L., Ku, Z., Liu, T., Rong, Y., Xu, M.M., Hu, M., Chen, J., Yang, Y., Grätzel, M., Han, H., Gratzel, M., Han, H., 2014. A hole-conductor-free, fully printable mesoscopic perovskite solar cell with high stability. Science. 345, 295–298. https://doi.org/10.1126/science.1254763

Meroni, S.M.P., Mouhamad, Y., De Rossi, F., Pockett, A., Baker, J., Escalante, R., Searle, J., Carnie, M.J., Jewell, E., Oskam, G., Watson, T.M., 2018. Homogeneous and highly controlled deposition of low viscosity inks and application on fully printable perovskite solar cells. Sci. Technol. Adv. Mater. 19, 1–9. https://doi.org/10.1080/14686996.2017.1406777

Palma, A.L., Matteocci, F., Agresti, A., Pescetelli, S., Calabrò, E., Vesce, L., Christiansen, S., Schmidt, M., Di Carlo, A., 2017. Laser-Patterning Engineering for Perovskite Solar Modules with 95% Aperture Ratio. IEEE J. Photovoltaics 7, 1674–1680. https://doi.org/10.1109/JPHOTOV.2017.2732223

Philip, B., Jewell, E., Worsley, D., 2016. The impact of solvent characteristics on performance and process stability of printed carbon resistive materials. J. Coatings Technol. Res. 13, 911–920. https://doi.org/10.1007/s11998-016-9802-8

Poli, I., Baker, J., Mcgettrick, J., Rossi, F. De, Eslava, S., Cameron, P.J., 2018. Screen printed carbon CsPbBr3 solar cells with high open-circuit photovoltage. J. Mater. Chem. A. 38, 18677–18686. https://doi.org/10.1039/c8ta07694d

Priyadarshi, A., Haur, L.J., Murray, P., Fu, D., Kulkarni, S., Xing, G., Sum, T.C., Mathews, N., Mhaisalkar, S.G., 2016. A large area (70 cm ^{2}) monolithic perovskite solar module with a high efficiency and stability. Energy Environ. Sci. 9, 3687–3692.

https://doi.org/10.1039/C6EE02693A

Rakocevic, L., Gehlhaar, R., Merckx, T., Qiu, W., Paetzold, U.W., Fledderus, H., Poortmans, J., 2017. Interconnection Optimization for Highly Efficient Perovskite Modules. IEEE J. Photovoltaics 7, 404–408. https://doi.org/10.1109/JPHOTOV.2016.2626144

Liu,S., Huang,W., Liao,p., Pootrakulchote,N., Li, H., Lu, J., Li, J., Huang, F., Shai, X., Zhao, X., Shen, Y., Cheng, Y.,Wang, M., 2017. 17% efficient printable mesoscopic PIN metal oxides framework perovskite solar cells using cesium-containing triple cation- perovskite. J. Mater. Chem. A. 5,22952-22959. https://doi.org/10.1039/C7TA07660F

Van Deelen, J., Klerk, L., Barink, M., 2014. Optimized grid design for thin film solar panels. Sol. Energy 107, 135–144. https://doi.org/10.1016/j.solener.2014.05.028

Yang, M., Kim, D.H., Klein, T.R., Li, Z., Reese, M.O., Tremolet De Villers, B.J., Berry, J.J., Van Hest, M.F.A.M., Zhu, K., 2018. Highly Efficient Perovskite Solar Modules by Scalable Fabrication and Interconnection Optimization. ACS Energy Lett. 3, 322–328. https://doi.org/10.1021/acsenergylett.7b01221

Yang, W.S., Park, B.W., Jung, E.H., Jeon, N.J., Kim, Y.C., Lee, D.U., Shin, S.S., Seo, J., Kim, E.K., Noh, J.H., Seok, S. Il, 2017. Iodide management in formamidinium-lead-halide-based perovskite layers for efficient solar cells. Science. 356, 1376–1379. https://doi.org/10.1126/science.aan2301